Journal of Materials Research and Technology 30 (2024) 4248–4260

Contents lists available at ScienceDirect

Journal of Materials Research and Technology

journal homepage: www.elsevier.com/locate/jmrt

The role of the preparation route on microstructure and mechanical properties of AlCoCrFeNi high entropy alloy

Petr Kratochvíl [a,*], Filip Průša [a], Hana Thürlová [a], Angelina Strakošová [a], Miroslav Karlík [b], Jaroslav Čech [b], Petr Haušild [b], Jiří Čapek [b], Ondřej Ekrt [c], Markéta Jarošová [c], Marek Vronka [c], Jozef Veselý [d], Peter Minárik [d], Ondřej Jankovský [e], Marcello Cabibbo [f]

[a] University of Chemistry and Technology, Department of Metals and Corrosion Engineering, Technická 5, 166 28 Prague 6, Prague, Czech Republic
[b] Czech Technical University in Prague, Faculty of Nuclear Sciences and Physical Engineering, Trojanova 13, 120 00 Prague 2, Czech Republic
[c] Institute of Physics of the Czech Academy of Sciences, Na Slovance 1999/2, 182 21 Prague 8, Czech Republic
[d] Charles University, Faculty of Mathematics and Physics, Ke Karlovu 5, 121 16, Czech Republic
[e] University of Chemistry and Technology, Department of Inorganic Chemistry, Technická 5, 166 28 Prague 6, Czech Republic
[f] DIISM, Università Politecnica delle Marche, Via Brecce Bianche, Ancona, 60131, Italy

A B S T R A C T

Nearly equiatomic AlCoCrFeNi alloy samples were prepared by induction melting and mechanical alloying (MA) combined with spark plasma sintering (SPS). The cast sample showed a dendritic microstructure composed of spinodally decomposed nanometric constituents of the B2 and BCC phases. The spark plasma sintered sample exhibited an ultrafine-grained microstructure of B2 phase and FCC solid solution and $Cr_{23}C_6$ carbides. The MA + SPS sample was strengthened by compressive stress-strain test up to a yield strength of 2029 ± 5 MPa, resulting significantly higher compared to 1366 ± 32 MPa of the cast sample. In addition to the higher compressive yield strength, the sintered sample exhibited a hardness of more than 130 HV higher compared to the cast alloy. On the other hand, the cast alloy showed high plastic deformation (29%) and significantly high ultimate compressive strength of 3072 ± 122 MPa. Together with these mechanical characteristics, the MA + SPS sample showed good thermal stability while preserving the mechanical properties even after annealing at 800 °C. This was not the case with the cast sample, in which ductility and ultimate strength significantly decreased upon annealing at 800 °C. A substantial yield strength reduction of both MA + SPS and cast samples was recorded when tested at 800 °C. Nevertheless, stress-strain curve trends were observed to be quite different between the two samples, thus suggesting dissimilar deformation mechanisms under high-temperature compression.

1. Introduction

High entropy alloys (HEA) have been gaining their position in the field of materials research since 2004 [1]. Thenceforth, the number of publications concerning these alloys is growing intensely every year. This is caused by a rather revolutionary concept of alloy design combining four or more elements in near equiatomic quantities compared to the majority of the presently used alloys, which are based on one main element. HEAs proved to be attractive in material research not only for mechanical properties [2–4] but also for corrosion resistance [5–7] or specific magnetic properties [8–10] as well. Starting from CoCrFeNiMn alloy, the research spectrum broadened to different alloy compositions, resulting in a whole new material research segment containing an immense variety of alloys, where the desired properties can be tailored by varying the amount of one or more elements.

One of the alloys derived from the CoCrFeNi system is AlCoCrFeNi, which exhibits a transition in the phase composition with the amount of Al [11,12]. It shows the presence of only FCC solid solution when the molar ratio of Al is lower than 0.45. In the interval of 0.45–0.88, the microstructure is composed of a combination of FCC and BCC solid solutions and higher amounts of Al result in the complete transformation to BCC solid solution. However, the transition interval width differs depending on the processing of the alloy [11]. The phase transition is closely connected to a significant rise in hardness [13]. An increment of the Al molar ratio leads to higher lattice distortion and strengthening of the alloy, increasing the hardness of the alloy up to 740 HV when the molar ratio reaches a value of 3 [14]. The BCC solid solution in the cast alloys spinodally decomposes into ordered B2 and disordered A2 phases.

* Corresponding author.
E-mail addresses: kratochs@vscht.cz (P. Kratochvíl), prusaf@vscht.cz (F. Průša), thurlovh@vscht.cz (H. Thürlová), Angelina1.Strakosova@vscht.cz (A. Strakošová), miroslav.karlik@fjfi.cvut.cz (M. Karlík), jaroslav.cech@fjfi.cvut.cz (J. Čech), petr.hausild@fjfi.cvut.cz (P. Haušild), jiri.capek@fjfi.cvut.cz (J. Čapek), ekrt@fzu.cz (O. Ekrt), jarosova@fzu.cz (M. Jarošová), vronka@fzu.cz (M. Vronka), Jozef.Vesely@mff.cuni.cz (J. Veselý), Peter.Minarik@mff.cuni.cz (P. Minárik), Ondrej.Jankovsky@vscht.cz (O. Jankovský), m.cabibbo@staff.univpm.it (M. Cabibbo).

https://doi.org/10.1016/j.jmrt.2024.04.090
Received 21 November 2023; Received in revised form 15 March 2024; Accepted 10 April 2024
Available online 16 April 2024

The B2 phase is enriched with Al, Ni, and Co, reflecting significantly negative mixing enthalpies of Al–Ni and Al–Co, whereas the A2 phase is enriched in Fe and Cr [12]. The phase composition of mechanically alloyed (MA) and sintered AlCoCrFeNi alloy is not in overall agreement, as stated in the literature. The MA is a strongly non-equilibrium process during which metastable phases are formed, and consequently, the phase composition of alloys prepared with PM is highly dependent on the processing parameters. The combination of FCC and BCC solid solutions, as well as the decomposition of the BCC phase into σ or both σ and α' phases in sintered alloys, are reported [15–17]. As a consequence of such variating phase composition, post-process annealing can be applied to achieve a sort of equilibrium state of the material. Munitz et al. [18] showed an effect of short-term annealing on the phase composition of the cast alloy. Phase transformations started to occur at temperatures above 650 °C, at which both FCC and σ phases occurred. The σ phase dissolved above 975 °C, whereas FCC was stable until 1100 °C [18,19], but eventually, it was found that at 1200 °C, the majority of the phases were dissolved in the BCC solid solution [18]. Nevertheless, exceeding the maximum solubility level led to precipitation of the B2 phase during cooling.

Regarding mechanical properties, the AlCoCrFeNi outperforms most of the other CoCrFeNi-based alloys, particularly in yield and ultimate strengths. Cast specimens reach compressive yield strength (CYS) and ultimate compressive strength (UCS) above 1200 MPa and 2000 MPa, respectively, with more than 15% of plastic strain [20,21]. The considerably high plastic strain provides space for reinforcing this alloy to achieve even better mechanical properties. Alloy prepared with the PM technique shows an even higher CYS value of 2400 MPa with UCS 2780 MPa [17]. Interesting behaviour was observed when the stress-strain diagram was measured at cryogenic temperature. The alloy showed a rise in the CYS and the UCS with almost no decrease in plasticity [20]. A similar phenomenon was observed for the CoCrFeNiMn alloy tested at cryogenic temperatures [22].

Other Al-containing multi-phase high entropy alloys, apart from the Cantor-based Al alloy, are studied for their phase composition and mechanical properties. Replacing Co, Cr and Ni with Al, Cu, Ti or Si to lower the overall price of the prepared alloys [23]. Alloys based on AlFeCuSiX show a variation of phases depending on the last added element and high values of microhardness reaching from 890 to 1150 HV 2 [24]. Regarding the compression tests highest results were achieved with X = Cr, reaching CYS of 1570 and UCS 2070 MPa [25].

As mentioned before, phase composition, microstructure and mechanical properties are strongly dependent on the fabrication route of the alloy. Utilising a powder metallurgy approach could be highly beneficial for the mechanical properties of the alloy compared to conventional casting procedures. Enhancing the mechanical properties of AlCoCrFeNi alloy is of interest for possible industrial applications, with a combination of excellent oxidation resistance has predispositions for high-temperature applications, e.g. automotive or aerospace engine components, heat-exposed powerplant components etc. In this work, two specimens of the AlCoCrFeNi alloy were prepared with different methods, by an ultrashort-term MA followed by a spark plasma sintering (SPS) compaction and by induction melting. Both specimens were examined in terms of phase composition, microstructure, and mechanical properties to compare the preparation methods and their influence on the microstructure and mechanical properties of the alloys.

2. Materials and methods

One of the AlCoCrFeNi alloy specimens was prepared by short-term MA with subsequent SPS compaction. Pure powders of each element (Co 99.8%, Cr 99%, Fe 99.9%, Ni 99.5%, Al 99.7%) were used in appropriate amounts to prepare the equiatomic alloy. A total amount of 20 g of the powder mixture was put in the jar along with milling balls, both made from AISI 420 stainless steel. The balls-to-powder weight ratio was 1:15. To decrease the undesired cold welding, 4 wt% of n-heptane was used as the process control agent (PCA). The sealed vessel was then flushed with argon of 99.996 purity (2 l min^{-1} for 2 min) to prevent any oxidation during the alloying process. The MA was carried out in 30 min intervals followed by 10 min breaks between them until the straight time of the MA reached 8 h. The rotation speed was 400 rpm.

The prepared powder alloy was sintered in SPS device FCT Systeme HP D 10. An amount of 10 g of the powder was put in a graphite mould with a diameter of 20 mm and sealed with graphite paper. The sintering temperature was set to 1000 °C with a heating speed of 200 °C min^{-1} and a pressure of 48 MPa being applied after reaching the sintering temperature. The sample was held under these conditions for 10 min, which prevents excessive coarsening of the microstructure. Eventually, the sample was cooled down to laboratory temperature with the maxima cooling speed of the machine, which is determined by the temperature gradient between the mould and both the water-cooled pistons of the SPS machine.

The other AlCoCrFeNi specimen was prepared by induction melting. Small chunks of the individual base metals in precise weight ratios were melted in an Al_2O_3 crucible at 1800 °C under an argon atmosphere. The melted alloy was homogenized by eddy currents for several minutes before casting. Afterwards, the alloy was cast in a steel mould 14 mm in diameter.

The chemical composition and phase composition of the samples were determined with X-ray fluorescence spectroscopy (XRF, PAN-analytical Axios) and X-ray diffraction spectrometry (XRD, PAN-analytical X'Pert PRO, Co Kα, λ = 1.7903 Å), respectively. The C and O analyses were performed with an electron probe microanalyzer JXA-8230 JEOL with LaB6 cathode equipped with five wavelength-dispersive X-ray spectrometers. Quantitative processing was performed using standards (CuO for O and SiC for C) and calculation by the XPP method of Pouchou and Pichoir.

The microstructure was examined with light microscopy (LM, Nikon ECLIPSE MA 200), including the surface porosity, which was evaluated with the colour threshold method in ImageJ software. A more detailed examination was performed with scanning electron microscopy (SEM, Tescan Lyra, 20 kV) together with electron dispersive spectroscopy (EDS, OXFORD Instruments INCA 350, 80 mm^2), and (scanning) transmission electron microscopy ((S)TEM, JEOL JEM-2200FS, 200 kV) equipped with energy dispersion spectrometer (EDS, JEOL Centurio) and NanoMEGAS ASTAR precession diffraction unit. Thin foils from the cast material were electropolished (T = −30 °C, U = 15 V) in a TENUPOL 5 (Struers) unit filled with a solution of 20% HNO_3 in methanol, a lamella from the sintered alloy was prepared by a Ga + focused ion beam (FIB, FEI Quanta DualBeam).

Mechanical properties were examined by the Vickers hardness and compressive stress-strain tests. The hardness was measured with a load of 30 kg and a load time of 10 s. The average value was calculated after measuring 10 indents. The compressive tests were performed on the LabTest 5.250SP1-VM machine using block-shaped specimens with a height corresponding to 1.5 times the side of the base. The deformation speed was set to 10^{-3} s^{-1}, and each alloy was tested using at least three samples to provide sufficient statistical reliability. The compressive tests were performed at room temperature, at 800 °C, and at room temperature after being annealed at 800 °C for 100h.

3. Results and discussion

3.1. Chemical composition

The chemical composition of the samples was examined using XRF analysis. The results are shown in Table 1, from which it can be seen that although prepared by such different methods, both samples had similar chemical compositions. All the elements except Al are around the desired equiatomic composition. The lower amount of Al, which was slightly below 17 at.%, could be ascribed either to the pre-oxidized Al powder particles or to its oxidation during the preparation processes

Table 1
The element composition (in at.%) of the cast and sintered AlCoCrFeNi samples (XRF).

	Al	Co	Cr	Fe	Ni
Cast	16.3	20.8	19.6	20.7	22.5
MA + SPS	16.7	19.8	18.6	22.8	22.0

since it has the highest affinity to the oxygen of the present elements. However, the induction casting, as well as the MA, was performed under an Ar atmosphere to prevent any unsolicited oxidation, and the sintering process was done in a vacuum. There is a possibility that the used materials were pre-oxidized in their raw form, but that would not cause a decrease of more than 3 at.%, and this effect should be more emphasized in the MA + SPS process considering fine powders used for this process compared to small chunks for induction casting. Another reason for the lower Al content in both samples may be the absorption of the Al signal in other elements with higher atomic numbers. On the other hand, the MA + SPS alloy showed a slightly increased content of Fe, which is associated with the sudden hardness increase due to a formation of intended phases, which are characterized by significantly higher hardnesses compared to individual powders. This increases the wear rate of the alloying jar, foremostly increasing the content of Fe, which is also shown in Table 1.

3.2. Phase composition and microstructure

The phase composition of prepared specimens was determined using XRD (Fig. 1). The cast alloy was double-phased, formed of BCC (A2) phase and B2 ordered cubic phase identified as Al($Ni_{0.5}Co_{0.5}$) (ICDD card no. 01-071-5682, space group Pm-3m). Both phases were also detected by electron nanodiffraction, as will be shown further. That is in good agreement with other works on AlCoCrFeNi research, which frequently report the presence of the B2 phase along with other phases [4,26–31]. As shown in the difractogram (Fig. 1), the cast alloy is formed of the disordered BCC A2 (ICDD card no. 04-004-9051, space group Im-3m) and ordered B2 phase originating from the spinodally decomposed BCC solid solution of the cast alloy [12]. These two phases are represented with the same reflections, as both have the BCC crystal structure. Hillel et al. [29] mentioned in their work that it is impossible to differentiate between the single B2 phase and B2/BCC mixture. These two phases are non-distinguishable with bulk XRD as the main peaks referring to the planes (110), (200), and (211) overlap, and other B2 superlattice reflections (111), (012) have a low intensity to be distinguishable with a bulk XRD.

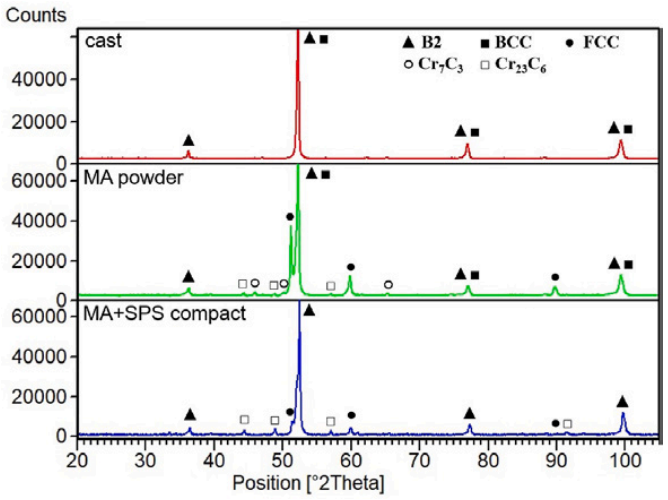

Fig. 1. The XRD diffractograms of the cast, MA, and sintered AlCoCrFeNi alloy.

On the other hand, the MA powder alloy consisted of a mixture of B2, BCC, and FCC (ICDD card no. 04-022-2301, space group Fm-3m) phases. The B2 phase was found to be the same type of Al($Ni_{0.5}Co_{0.5}$) as in the cast alloy. In addition to the B2 and A2 phases, the FCC phase was present as well, which is commonly found in cast alloys with an aluminium content lower than approximately 18 at.% [12]. Considering the actual amount of aluminium in the MA + SPS compact being 16.7 at.%, the presence of the FCC phase is reasonable, although it was not present in the cast alloy with an even lower aluminium content of 16.3 at.%. Considering the amount of Al reaching up to 16.3 at.%, the content of residual FCC phase might be, considering the measurement error of XRF analysis, below the detection limit of XRD. The presence of the B2 phase was not reported in the MA AlCoCrFeNi alloys [15,16,49]. Residues of this phase were present in the MA $AlCoCrFeNi_{0.3}$ [30] and in the equiatomic atomized alloy [32]. Otherwise, the MA powder alloys are formed of BCC or a combination of FCC and BCC solid solutions [15,16]. A small amount of chromium carbides was also detected in the powder alloy, which comes from the use of n-heptane as the PCA. Compared to the MA + SPS sample, there is a certain difference in the diffraction pattern of the sintered and powder samples. The reflections belonging to the FCC have a lower intensity in the compacted sample, resulting in a decrease in the FCC fraction in the sample. On top of that, no BCC solid solution was detected in the sintered sample, which might be caused by the complete overlapping of the characteristic peaks of the present B2 and the BCC phase, which is reported in the work of others [15,17]. Thus, the presence of either B2 or BCC solid solutions considering the residual stress strains, which affects distortion of the crystallographic lattices of both phases, is even more difficult to resolve within such a prepared alloy. The situation is further complicated by a partial relaxation of the lattice strain during the sintering process, although the sample is compacted only for a very short time. The change of the lattice parameters could shift the BCC phase reflections, resulting in their superposition with the reflections of the B2 phase. The Cr_7C_3 carbides in the powder alloy transformed during the sintering process to $Cr_{23}C_6$, a more thermodynamically stable form [33].

The LM micrographs of the MA, MA + SPS, and cast alloys are shown in Fig. 2. At first sight, there is an evident difference between the preparation methods. Fig. 2a is a micrograph of the 8h MA powder alloy. The microstructure of the particle is rather homogeneous, with several voids due to the continuous intensive plastic deformation and mutual fragmentation of the powder particles. Differences in contrast are associated with different phases or crystallographic orientations. The ultrafine-grained microstructure of the MA + SPS sample is in Fig. 2b, which shows a good homogeneity with non-distinguishable grains in the LM micrograph. Comparing Fig. 2a and b demonstrates the reduction of the porosity during the SPS process, which, together with no visible particle boundaries in the MA + SPSed sample, indicates an overall good optimization of the sintering parameters. The microstructure of the MA + SPSed sample is significantly more refined than the cast sample (Fig. 2c). In addition, the average surface porosity of the MA + SPSed sample is also lower when compared to the cast specimen, although both samples showed extremely low porosity under 0.25%. On the contrary, the cast sample (Fig. 2c) shows an equiaxed dendritic microstructure with an average grain size of around 80 μm. Along the dendrite, there is a zone of darker grey colour, signifying a slightly different chemical composition caused by the coring effect, while the interdendritic region is of a lighter shade. These findings are coherent with previous results mentioned in Refs. [12,27].

SEM micrographs representing the microstructural constituents are in Fig. 3. Fig. 3a presents the homogeneous, ultrafine-grained microstructure of the MA + SPSed sample with grains of an average diameter of around 500 nm. At least three different phases can be differentiated by the chemical contrast of backscattered electrons, which is in good agreement with the XRD results (Fig. 1), showing 4 phases in total. Noticeable black dots are pores, which were enlarged during the chemical etching of the sample. This distinct microstructure, where

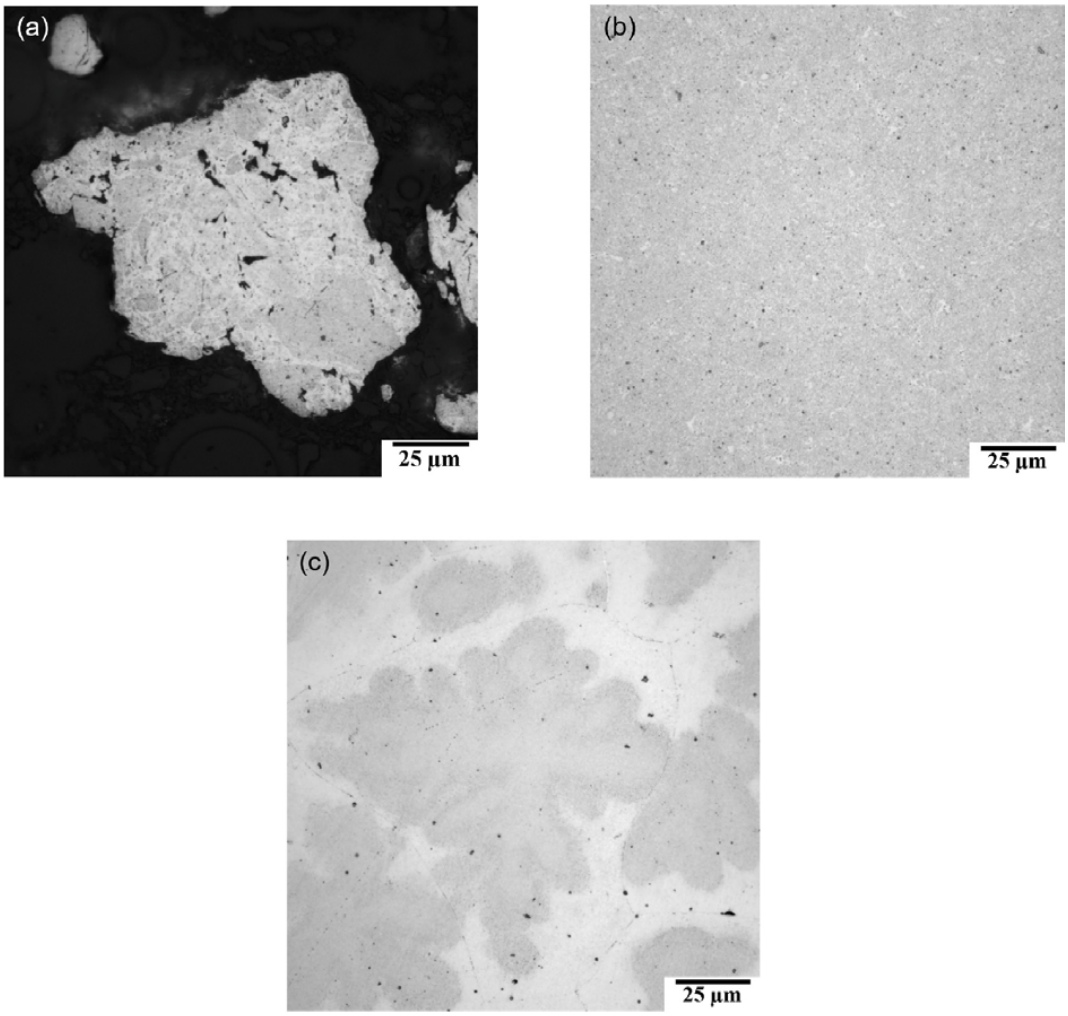

Fig. 2. The LM micrographs of AlCoCrFeNi alloy prepared by: a) MA (powder form); b) MA + SPS; c) induction casting after etching.

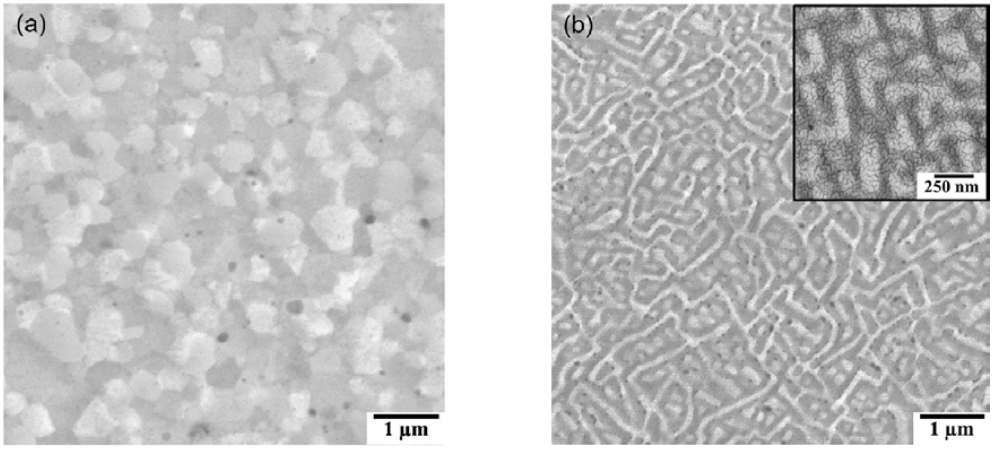

Fig. 3. The SEM micrographs of the AlCoCrFeNi alloy prepared by: a) MA + SPS; b) induction casting.

grains have discernible boundaries, was not described in other papers [15–17]. Comparing the LM micrographs, the microstructure is similar to Ji et al.'s work [15], although the SEM image was not provided. However, the microstructure in Ref. [15] is composed of grains up to 200 nm, stating the FCC phase has larger grains compared to the grains of BCC. Increased microstructural refinement is caused by a lower sintering temperature of 900 °C compared to our work (1000 °C), as well as by the longer MA being 60 h in total. The paper of Mohanty et al. [16] reports a microstructure with apparent powder-to-particle boundaries, although sintered at the same temperature (1000 °C) as in our work. The cast sample (Fig. 3b) exhibits two distinct but subtle phase constituents with a maximal width of 100 nm. These phases seem to be interconnected, with cuboidal precipitates in between, but at higher magnification (upper right corner of the micrograph), it is evident that it

represents a matrix with cervical-shaped precipitates, a typical modulated plate spinodal structure. The SEM micrograph confirms the existence of two phases (B2 and BCC) discussed in the previous paragraph.

This microstructure formed by spinodal decomposition is common for cast AlCoCrFeNi alloys [11,12,27,34,35]. The spinodal decomposition also occurs in other HEA systems containing Al and Ni [36,37], but it is reported to appear in alloys with different compositions as well [38–40]. The difference in size and morphology of the spinodally decomposed phases B2 and BCC in the dendritic core and the interdendritic region was not observed, so only one SEM micrograph is shown in Fig. 3b. However, in the literature, dendritic and interdendritic regions in cast AlCoCrFeNi alloys are frequently reported to have different microstructure [21,26,27,34]. A slight difference was observed only in the chemical composition (Fig. 4), where the dendrite core is enriched in Ni and Al, and the interdendritic region, close to grain boundaries, is enriched in Cr. This is in good agreement with the work of others [21,26,27]. Visible black spots are enlarged pores or holes emerged during electrolytic polishing of the sample.

The SEM + EDS distribution maps of elements of MA + SPSed and cast alloys are shown in Fig. 5. The MA + SPSed sample is homogeneous with more or less uniform distribution of alloy constituents, although grains enriched in Cr are apparent, whereas the concentration of other elements is decreased in these regions (Fig. 5a). Increased concentration of Cr is most probably connected with the formation of carbides in the sintered samples, as was shown by the XRD analysis (Fig. 1). This would also correspond to the depletion of the rest of the elements because element with the second highest tendency to form carbides would be Fe, but there is no evidence of higher concentration of Fe in the same regions as Cr. Nevertheless, the regions with higher Fe concentrations are present, but they seem to have larger dimensions compared to the grains. The most uniform distribution has Co, whose concentration is slightly lowered in the Cr-rich grains.

The SEM + EDS element distribution map of the cast alloy is in Fig. 5b. When compared with the MA + SPSed sample, the microstructure is completely different. The element distribution confirms the existence of two phases with dissimilar chemical compositions. The matrix depicted with a darker shade of grey is enriched in Al and Ni, and hence, it represents the B2 phase. Opposite to this phase, the bright precipitates show increased amounts of Cr and Fe, and thus it represents

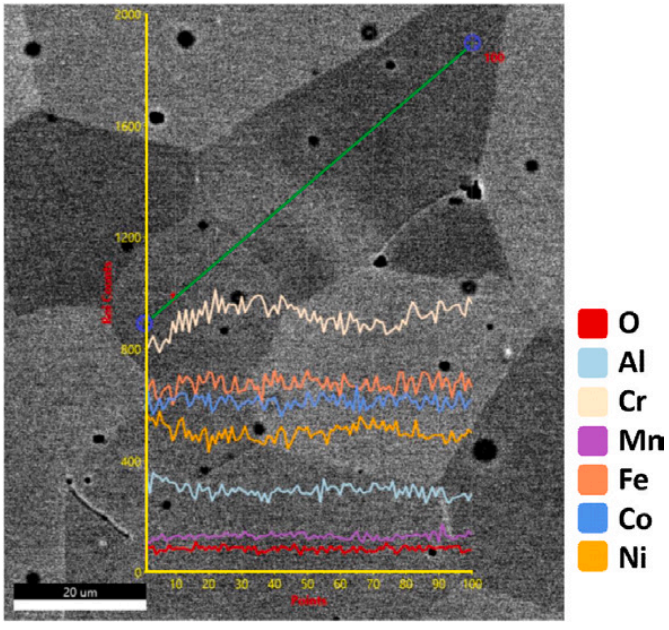

Fig. 4. The cross-grain boundary EDS line analysis of the cast AlCoCrFeNi alloy.

the complementary BCC (A2) phase. High mixing enthalpy of the Al–Ni pair diminishes the configuration entropy effect and tends to form ordered B2 phases rather than disordered solutions. As opposed to this, segregation of the Fe–Cr-rich precipitates takes place in the B2 matrix, which was already demonstrated in precedent works [12,21,27,34]. The only homogeneously distributed element among the analyzed area is Co.

The microstructure of both samples at a finer scale was examined by TEM/STEM. Fig. 6a shows a detail of the spinodally decomposed microstructure in the dark-field TEM image using the $(010)_{B2}$ spot of the cast alloy. The B2 matrix thus appears bright, and the disordered BCC precipitates, with a maximal width of 100 nm, are dark. The MA + SPSed sample shows a completely different microstructure. From the STEM high-angle annular dark-field (HAADF) image (Fig. 6b) taken at the same magnification it follows that the alloy is reinforced by a dense distribution of Al_2O_3 particles, having in the majority under 30 nm in diameter. The grain and phase boundaries cannot be well distinguished in the STEM-HAADF micrographs, so an Automated Crystal Orientation Mapping (ACOM) NanoMegas precession diffraction system was used to obtain phase and grain distribution maps (Fig. 7). From the phase map (Fig. 7a) it follows that the identified phases are FCC (green), B2 (red) and $Cr_{23}C_6$ (blue), points with no match are displayed as black. The grain size can be easily estimated from the grain orientation maps (Fig. 7b–d). The FCC phase grains and the $Cr_{23}C_6$ particles are around 500 nm in size, while the grains of the B2 phase were overall bigger, showing a certain level of mutual interconnections.

Fig. 8 presents the distribution of alloy constituents in the cast and MA + SPSed samples as found by STEM EDS. In agreement with the SEM-EDS results, the B2 ordered matrix in the cast alloy is rich in Ni, Al, and Co, while the BCC precipitates are rich in Cr and Fe (Fig. 8a). In the MA + SPSed alloy, the B2 phase has a similar composition, while the FCC phase is enriched in Fe and Co.

STEM EDS mapping enables obtaining not only a qualitative distribution of elements in the microstructure but also quantifying the composition of the microstructure components. The average values, obtained from 10 read-outs (pop-up areas marked in Fig. 8a and b) on several EDS maps of the investigated alloys, are given in Table 2.. From the quantification, it follows that the content of Co, Fe, Ni, and Al in the bright B2 phase in the cast sample is practically the same as it was measured in the interdendritic region by Wang et al. [21]. In the case of the dark BCC precipitates, our results match with [21] only for Co and Fe, while we measured nearly double Cr concentration and lower content of Ni and Al. If we compare the composition of the B2 phase in the cast and MA + SPSed sample, it is nearly identical, except for carbon and oxygen, which are not present in the cast alloy. Comparing the chemical composition of the latter main phases gives us about 20% higher content of Co, Fe, and Ni in the FCC solid solution in the MA + SPS sample, while the content of Al and Cr is roughly 50% lower than in the BCC phase of the cast alloy. Chromium in the $Cr_{23}C_6$ carbides is substituted by 10 at.% of Fe and 4 at.% Co, while the content of Ni, Al, and Si is significantly lower, ranging from 0.3 up to 1.5 at.%. Hence, the carbide should be more appropriately denoted as $M_{23}C_6$ (M = Cr, Co, Fe, Ni, Al). The majority of oxides are Al_2O_3, but particles containing chromium, iron, nickel, or silicon were found as well, which might correspond to the pre-oxidized powders used for their preparation. However, these results are often neglected in the recent works of others, although the usage of fine powders is often associated with some residual pre-oxidation, hardly to be dealt with.

Due to the presence of carbide and oxide particles in the MA + SPS alloy, the overall content of C and O was analyzed in both of the samples. For this purpose, WDS analysis with 15 readouts across the whole sample was used to obtain an average value. As expected, the content of both elements in the cast sample was below 2 at.% with the origin in contamination of input materials, considering also higher error percentage at lower concentrations. On the other hand, the concentration of O in the MA + SPS sample reached 4.13 at.%, although also originating as contamination of input powders, it resulted in the formation of

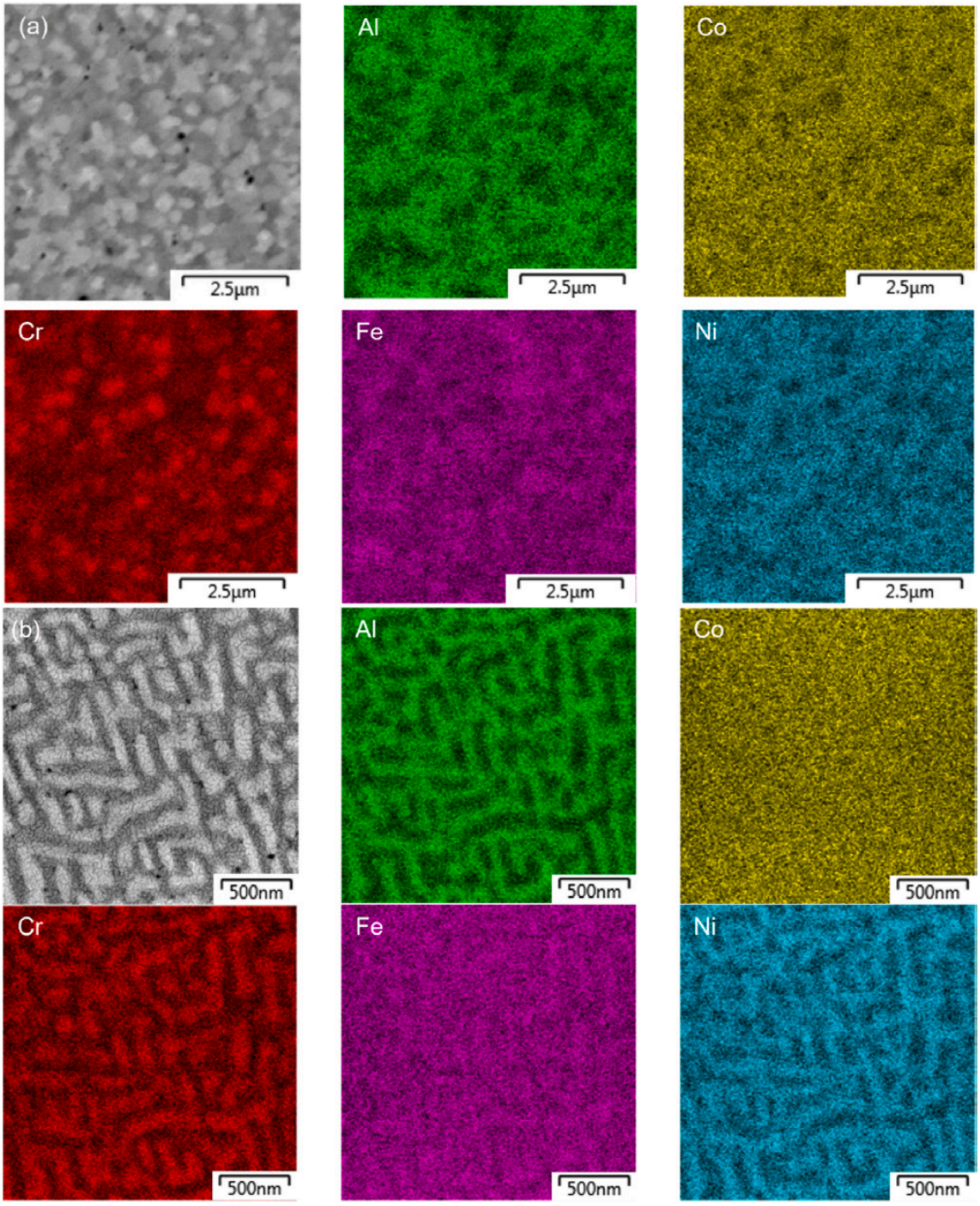

Fig. 5. The SEM + EDS distribution maps of elements in the MA + SPSed (a) and in the cast (b) AlCoCrFeNi alloy.

nanometric oxide particles in the sample. The content of C in the MA + SPS sample was as high as 7.36 at.%, corresponding with the amount of carbide grains in the material.

3.3. Mechanical properties

The overall results of mechanical properties are summarized in Table 3. The highest hardness (635 ± 4 HV 30) was achieved by the MA + SPS sample, exceeding the hardness of the cast alloy by 130 HV. This difference is caused mainly by the lattice distortion and internal strains accumulated during MA [41] that are partially maintained due to the short-term SPS compaction. Although the cast sample exhibits a more refined microstructure with constituents of about 100 nm wide, the main strengthening mechanism in the B2-A2 spinodal structure is the coherency strain strengthening of the matrix-precipitate interface. Considering the fine dimensions of present precipitates, the interactions between dislocations and precipitates result in a planar slip that does not provide enough strengthening to compete with the latter sample [42]. Compared to this, the MA + SPSed sample is composed of grains approximately two orders of magnitude smaller than the cast sample, which combined with other factors, has a higher impact on the resulting hardness. The carbides and oxides present in the MA + SPSed sample are another factor contributing to the hardness increase. The obtained hardness of the MA + SPSed sample is comparable with the results of Ji

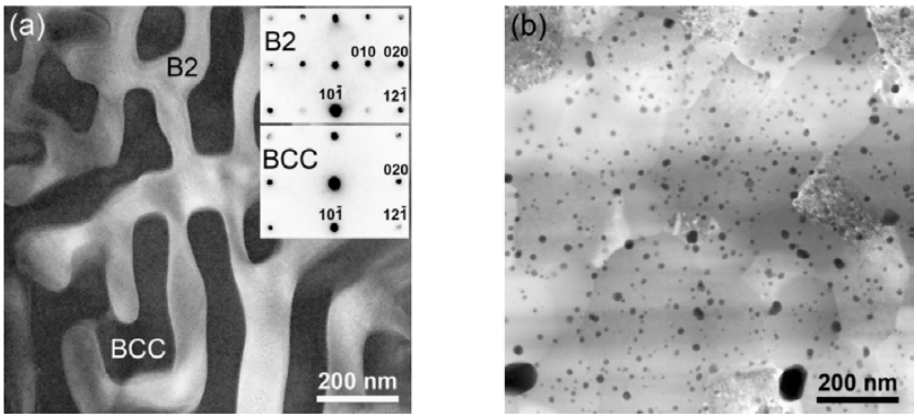

Fig. 6. TEM/STEM micrographs of the AlCoCrFeNi HEA: (a) Dark-field TEM in the (010) B2 spot of the cast alloy with nano diffraction patterns of the light B2 and dark BCC phases in the inset, (b) STEM high-angle annular dark-field (HAADF) of the sintered alloy; numerous black particles in (b) are oxides.

et al., reporting a hardness of 625 HV 10 [15]. Other papers record even higher hardness of MA + SPS samples, reaching the average values of 710 HV 5 [17] or even 815 HV 0.05 [16]. It has to be noted that all the above-mentioned samples were prepared by MA, lasting for 60 h, processes far exceeding the 8 h process duration used for the preparation of the alloys investigated in the present work. Thus, the longer MA led to a different phase composition, establishing the equilibria between mutually competing dynamic recovery and intensive plastic deformation in favour of higher imposed internal strains, as well as further grain refinement. The hardness of the cast sample was 504 ± 10 HV 30, which is in good accordance with the literature [11,27,43]. Considering the conformity of microstructure formation and phase composition, the main contribution to the hardness of the cast sample is the size of the microstructural constituents, which is in good accordance with the results of hardness reported by others [11,27,43].

The stress-strain tests were performed at different temperature conditions, which comprised testing at room temperature (RT) of the as-prepared samples and of samples that underwent annealing (100 h/800 °C) as well as samples being tested at an elevated temperature of 800 °C. The effect of lattice strain and grain size of the MA + SPS sample is demonstrated also in the stress-strain compressive curves measured at RT (Fig. 10a). The MA + SPS sample reached a CYS of 2029 ± 5 MPa, which is nearly 700 MPa higher than of the cast sample, which reached a CYS of 1366 ± 32 MPa. Certainly, the presence of carbides and oxides in the MA + SPS alloy, bearing the role of particle reinforcements, has also pushed the CYS to higher values. Nevertheless, higher CYS was accompanied by lower ductility, and, in this case, lower UCS as well due to present carbides and oxide nanoparticles. While the MA + SPSed alloy possessed still a decent plastic strain of nearly 9%, the cast sample fractured at a significantly higher plastic strain of 29%, reaching the UCS of 3072 ± 122 MPa. This corresponds to a value 400 MPa higher than that of the MA + SPS sample. Both the investigated alloys showed different work hardening rates (Fig. 9). The work hardening rate of the MA + SPS was higher right after the yielding point, nevertheless due to the present internal strain and strengthening particles, its decline was faster, and thus, it soon decreased below the work hardening rate of the cast alloy. According to the literature, those microstructural characteristics and other objections to the dislocation movement in the MA + SPS sample are the cause of jogging and anchoring the dislocations and thus hindering them in their movement. Therefore, the activation energy for the dislocation glide is higher compared to the cast sample, which corresponds with a higher yield strength of the MA + SPS sample. Interaction between the dislocations and other structural components is more intense in the cast sample and that results in a higher flow stress of the sample, whereas high stress in the MA + SPS sample causes overcoming of the objections e.g. by cross-slip, which results in dynamic recovery and therefore reduction of the hardening. The hardening rate of the cast alloy decreased in an atypical manner at an almost constant rate until cracking. However, the difference in the overall plastic deformation might be also attributed to the presence of B2 phase intermetallics, which are known for their RT brittle behaviour due to not meeting the Von Mises criteria having only <100> slip mode active [44]. Nevertheless, it was found that slip in the <111> direction is possible in other B2 intermetallics with low anti-phase boundary energy [45], which may be the case with B2 matrix in the AlCoCrFeNi as well as similar behaviour was found in different B2-BCC phase HEA [42]. The B2 phase ductility may be also enhanced with the activation of mechanical twinning observed in AlNi alloys [46,47].

The MA + SPSed sample outperformed the alloy reported by Ji et al. [15] but had slightly lower UCS than the alloy reported by Rogal et al. [17] while exhibiting higher ductility. However, both samples were prepared with long-term MA (35 and 60 h) and variating SPS compaction temperatures; Ji et al. used 900 °C for 10 min, whilst Rogal et al. sintered their sample at 1050 °C for 15 min. The beneficial effect of the MA with a combination of SPS can be demonstrated, for example, with the comparison with a cast sample reinforced with WC particles [48]. The strengthening of 60 wt% of WC resulted in the increase of CYS and UCS to 1709 MPa and 2091 MPa, respectively, which is still 300 MPa and nearly 600 MPa less than the values of the MA + SPS sample investigated in our work. Such results confirm that the MA + SPS parameters are well optimized and targeted on the mechanical performance of the alloys. Compared to the results of compressive tests of identical alloys obtained after 84 h of mechanical alloying, the UCS was significantly lower, reaching only 1947 MPa [49]. The CYS (1366 MPa) of the investigated cast alloy is comparable with the results of others ranging from 1209 MPa up to 1399 MPa [18,21,27,43], but the performance during the plastic stage is significantly different. Other alloys achieved a maximum UCS of 2065 MPa [18] compared to 3072 MPa reached in this work. More importantly, the total compressive strain was, in some cases, almost the same, which was probably caused by a slower deformation speed compared to ours 10^{-3} s^{-1}.

The significant difference in mechanical properties of the MA + SPS and cast alloy is based on the phase and microstructural composition of the compared alloys. It is generally known, that the strengthening of polycrystalline materials has four major contributions: solid solution strengthening, grain boundary strengthening, dislocation strengthening and precipitation/particle strengthening [50]. Solid solution strengthening in HEAs is based on severe lattice distortion because there is no major solvent element [27]. It cannot be certainly said that one of the samples has a more distorted lattice since both have similar chemical compositions. The spinodal decomposition of the cast sample could lead to a possible decrease in lattice distortion due to the formation of an ordered B2 phase, but the presence of the B2 phase was detected in the MA sample as well. On top of that, the TEM EDS results of chemical

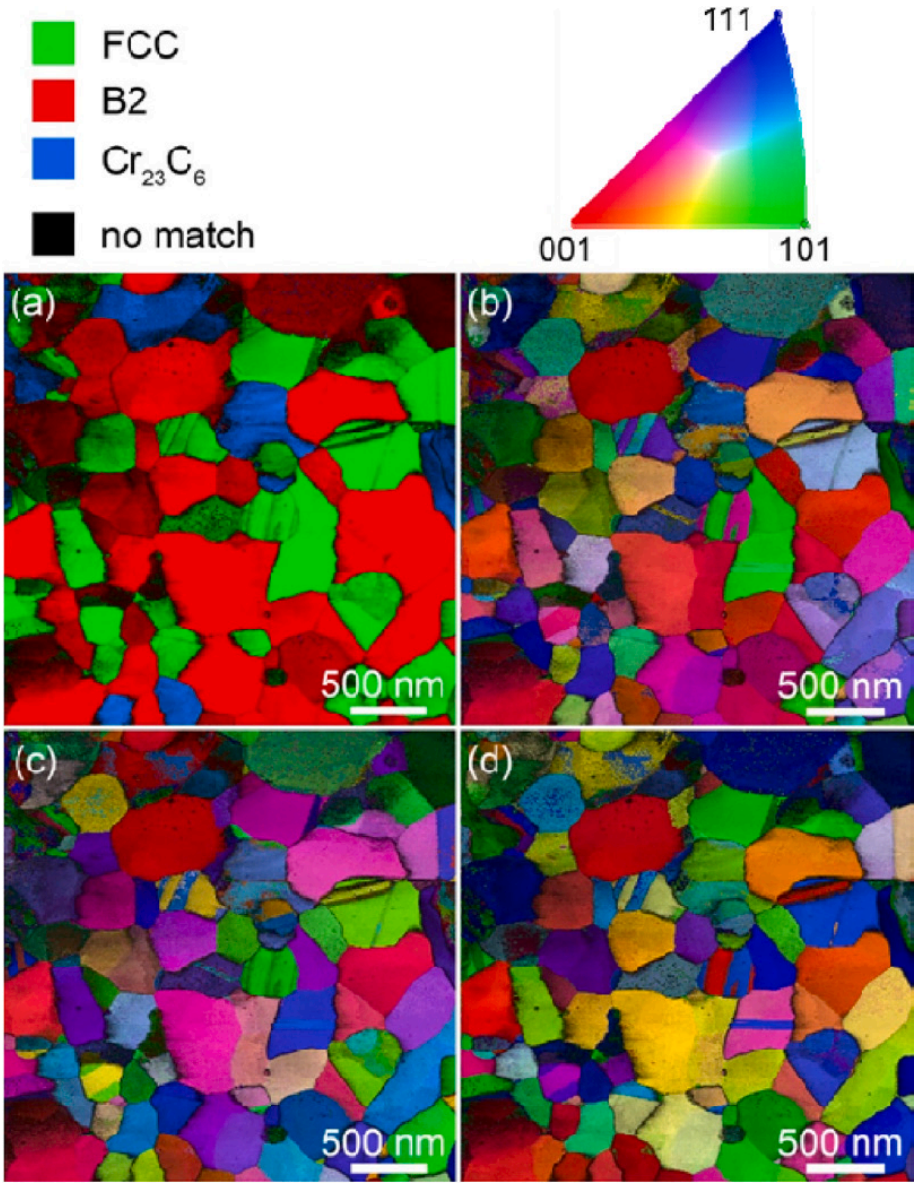

Fig. 7. ACOM TEM images of sintered AlCoCrFeNi HEA: (a) phase distribution map - the identified phases are denoted by green (FCC), red (B2 ordered BCC) and blue ($Cr_{23}C_6$) colours, points with no match are displayed as black, (b–d) grain orientation maps corresponding to the x-axis (b), y-axis (c) and z-axis - electron incidence (d); orientation maps are coloured according to the cubic inverse pole figure in the top part of the figure. (For interpretation of the references to colour in this figure legend, the reader is referred to the Web version of this article.)

composition (Table 2) did not reveal any essential differences leading to the solid solution strengthening. Nevertheless, it can be presumed that the MA + SPS sample has a more distorted lattice due to the nature of mechanical alloying, and thus it can benefit more from the solid solution strengthening. A similar principle can be applied to dislocation strengthening. Alloys prepared with MA have generally higher crystallographic defect density, therefore it can be presumed, that the dislocation strengthening is more significant in the MA + SPS alloy [51]. More evident is the effect of the grain boundary strengthening. Considerable differences in the grain size between the two samples favour the MA + SPS sample, which has two orders of magnitude smaller grains and thus a higher volume fraction of grain boundaries, which impede the dislocation movement. Since the microstructure of both samples is completely different, the precipitation strengthening has in either alloy different origin. The strengthening in the cast alloy is due to the spinodal decomposition based on the lattice constant mismatch between the A2 and B2 phases. Owing to the nanometric size of both phases, it has a remarkable impact on the yield strength of the alloy [27]. On the other hand, the MA + SPS sample contains $Cr_{23}C_6$ particles and mainly intragranular nanometric oxide particles causing a microstructural mismatch due to a difference in thermal expansion coefficients, which is applied during the high-temperature compaction, strengthens the alloy considerably [52].

Stress-strain tests after the annealing process (Fig. 10b) showed superior performance of the MA + SPS sample compared to the cast specimen. One can see that the curve after annealing of the MA + SPS sample is almost identical to the one obtained at RT (Fig. 10a). Both the CYS and UCS even slightly increased in value, see Table 3. The same cannot be said about the cast alloy, the nicely distinguishable transition around yielding point at RT transformed into the gradual transition from elastic to plastic deformation. The effect of the annealing on the cast alloy resulted in a major ductility reduction by 60% of the initial value. As a consequence, the UCS reduced to 2733 ± 111 MPa, showing an overall worse performance than the MA + SPS sample, which retained its performance. The XRD analysis after annealing (Fig. 11) showed no formation of new phases in the structure of the MA + SPS sample, except

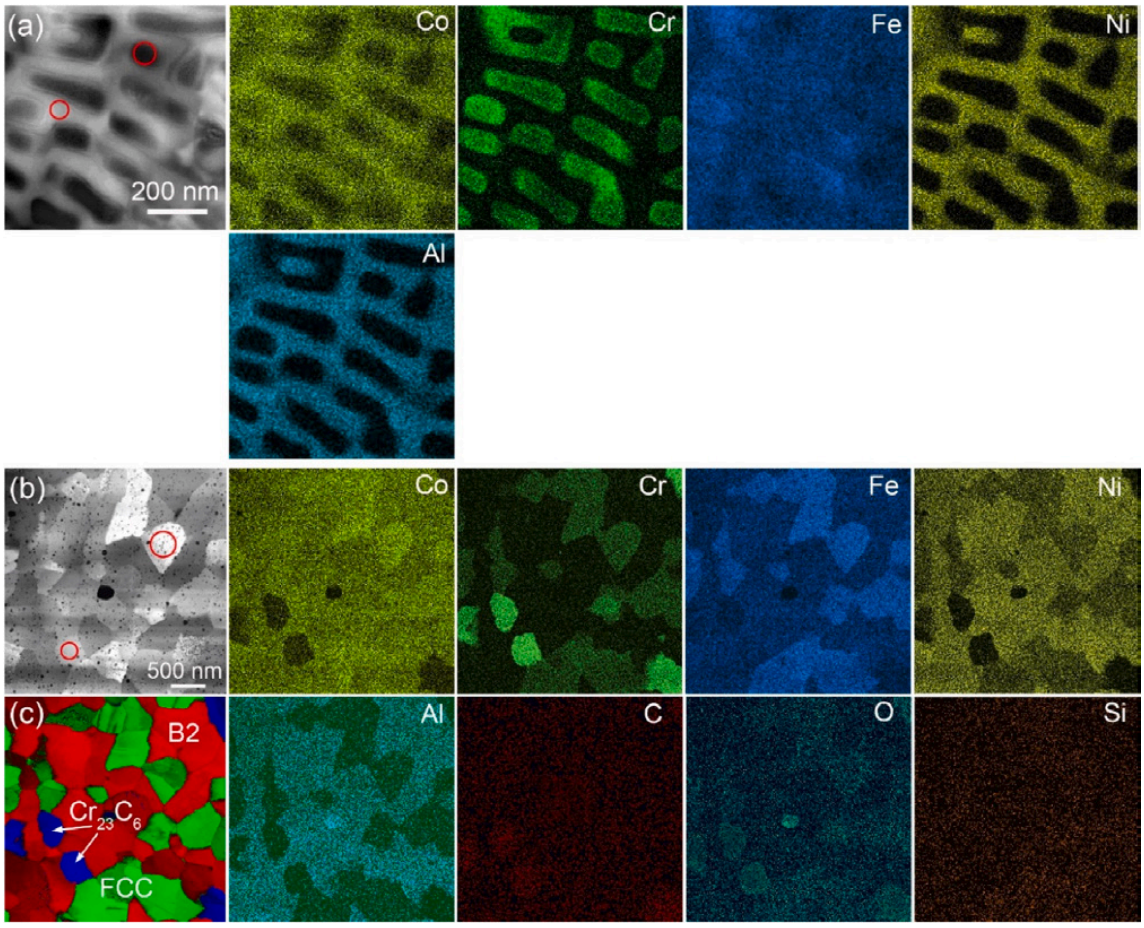

Fig. 8. STEM-HAADF micrographs (a, b), matching Automated Crystal Orientation Mapping (ACOM) phase map (c), and corresponding energy dispersive spectroscopy (EDS) maps of the cast (a) and sintered (b, c) AlCoCrFeNi high entropy alloy. Red circles in the inset in the micrographs (a, b) demonstrate pop-up areas used for the quantification of the chemical composition of relevant phases from EDS map data cubes; the results are summarized in Table 2. (For interpretation of the references to colour in this figure legend, the reader is referred to the Web version of this article.)

Table 2
The average composition (10 readouts) of the dark (Co, Ni, Al-rich) and bright (Cr, Fe rich) phase in the cast AlCoCrFeNi high entropy alloy and Fe-rich FCC phase, Ni-rich B2 ordered BCC phase, carbides $Cr_{23}C_6$, and oxides in the sintered alloy (MA + SPS) evaluated from TEM EDS maps (at.%).

Cast	Co	Cr	Fe	Ni	Al	Si	C	O
bright B2	21.5 ± 1.4	5.2 ± 1.1	16.5 ± 1.5	29.2 ± 2.8	20.3 ± 4.0	0.6 ± 0.4	–	–
dark BCC	18.6 ± 1.7	37.9 ± 8.9	28.3 ± 3.8	8.9 ± 6.5	5.1 ± 5.3	1.5 ± 1.9	–	–
MA + SPS	Co	Cr	Fe	Ni	Al	Si	C	O
FCC	22.2 ± 1.6	15.0 ± 0.4	34.3 ± 1.6	12.4 ± 0.5	3.0 ± 0.8	1.4 ± 0.3	8.3 ± 3.2	3.1 ± 1.6
B2	20.8 ± 1.7	4.2 ± 0.3	17.5 ± 1.3	26.8 ± 1.4	16.5 ± 1.3	0.8 ± 0.3	7.6 ± 1.1	5.7 ± 3.0
$Cr_{23}C_6$	4.0 ± 0.8	52.3 ± 3.2	10.6 ± 1.2	1.5 ± 1.4	1.4 ± 0.4	0.3 ± 0.3	30.0 ± 1.0	–
Oxides	3.2 ± 5.2	4.5 ± 5.1	3.5 ± 4.4	1.9 ± 2.2	20.9 ± 2.5	0.8 ± 1.5	14.8 ± 4.9	50.3 ± 17.9

Table 3
Summary of mechanical properties of the MA + SPSed and cast AlCoCrFeNi alloy accompanied by the confidence intervals.

Cast	CYS (MPa)	UCS (MPa)	HV 30
RT	1366 ± 32	3072 ± 122	504 ± 10
After annealing (800 °C 100h)	1448 ± 58	2733 ± 111	–
At 800 °C	322 ± 30	–	–
MA + SPS	CYS	UCS	HV 30
RT	2029 ± 5	2659 ± 106	635 ± 4
After annealing (800 °C 100h)	2119 ± 41	2782 ± 95	–
At 800 °C	147 ± 11	–	–

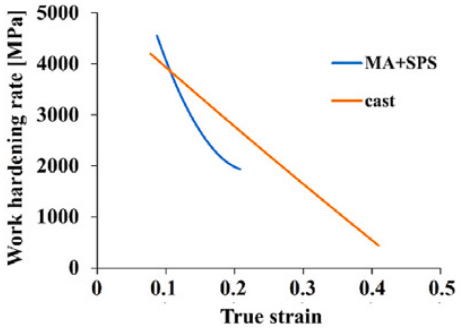

Fig. 9. Work hardening rate comparison of MA + SPS and cast AlCoCrFeNi.

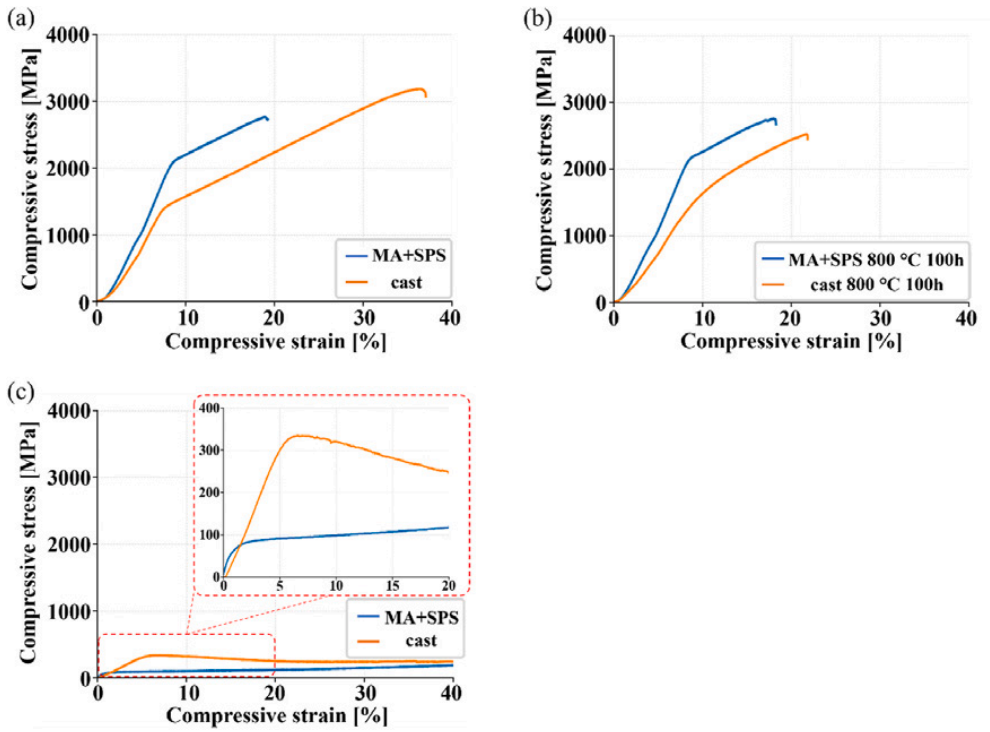

Fig. 10. The compressive stress-strain behaviour under different conditions comprising testing at a) RT; b) RT after annealing (800 °C 100h); c) elevated temperature of 800 °C (enlarged insight is marked by the red rectangle). (For interpretation of the references to colour in this figure legend, the reader is referred to the Web version of this article.)

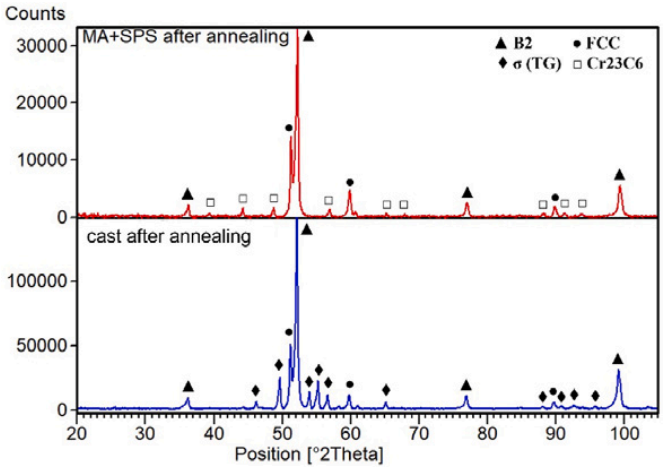

Fig. 11. The XRD diffractograms of MA + SPSed and cast AlCoCrFeNi alloy samples after annealing (800 °C/100 h).

for the change in the volume ratio of the FCC phase. Despite the rise in the volume fraction of the FCC phase by 10 %, the performance of the MA + SPS alloy was the same as prior annealing, confirming its exceptional thermal stability.

A significant difference is notable when observing the microstructure of the samples after annealing compared to the as-prepared state (Fig. 12). The increase in grain size is visible in both the investigated alloys, however, the coarsening of the microstructure is far more extensive in the cast sample, in which the BCC particles grew about five times their original size (Fig. 12d). Moreover, a different structure is visible in some of the BCC particles interior, showing a presence of a grey-white dotted particles, which corresponds to the σ-phase precipitation within these particles. Besides coarsening, the microstructure of the MA + SPS sample changed in general, making the present grains hardly distinguishable, which can be a consequence of a different after-annealing etching response.

The increase of the FCC fraction by 20 wt% in the MA + SPS alloy after heat treatment at 1000 °C for 2h was documented by Faraji et al. [53]. This increase resulted in enhanced ductility and an overall difference in compressive response. However, compared to an increase of the FCC phase by 10 wt% in our alloy was not enough to promote any change in the compressive behaviour. In theory, the microstructure coarsening along with an increased amount of the FCC should lead to an increase in ductility and reduction of strength characteristics, which was not shown during the compressive tests nor the thermal stability analysis. The hardness of the alloy was stable during the whole 100 h of annealing, and at the end, it even slightly rose. Since no new phase precipitation was shown by the XRD analysis, the microstructure after annealing was further examined with TEM (Fig. 13) as there was a possibility for σ-phase precipitation similarly to the cast sample. Neither the TEM proved the precipitation of the σ-phase as it is connected to the presence of the disordered BCC phase in the sample, which was not the case for the MA + SPS sample. Therefore, the thermal stability of the MA + SPS alloy is attributed to the presence of carbides and mainly homogeneously dispersed nanometric oxide particles. The oxide particles retained their size and density and thus limited any significant microstructural changes during the annealing. As the phase composition and microstructure are very similar to the as-prepared sample, the overall compressive response is almost the same compared to the initial RT-tested sample.

On the other hand, the phase composition of the cast sample underwent a significant change with a partial transformation of the BCC (A2) phase to the FCC phase and precipitation of the tetragonal (TG) Fe–Cr σ-phase (ICDD card no. 04-004-4324, space group $P4_2/mnm$) (Fig. 11). Precedent findings showed a formation of the FCC and σ-phase begin to occur at the interval of temperatures 550–650 °C at the grain boundaries of the B2-BCC microstructure [54,55], thus the main phase transformation takes place in the interdendritic region. As it was reported, the σ-phase precipitates were present in the form of round

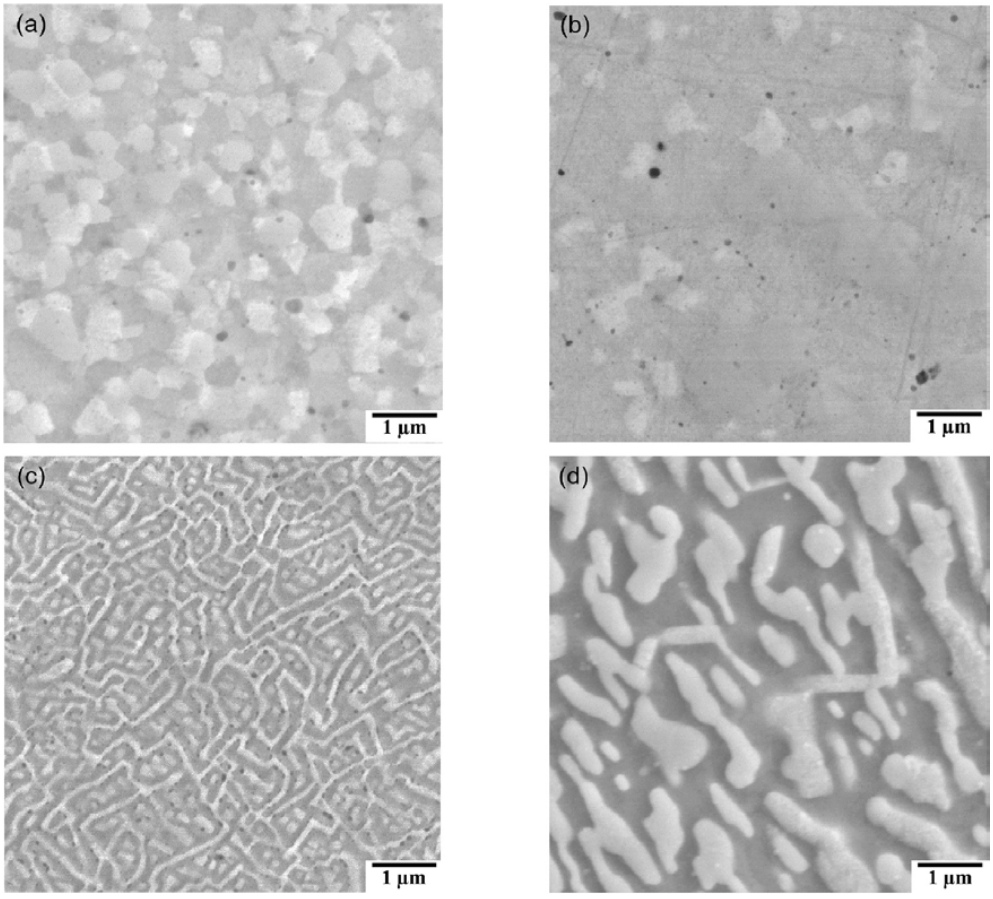

Fig. 12. The SEM micrographs of AlCoCrFeNi alloy prepared by: a), b) MA + SPS; c), d) induction casting (a, c represent the as-prepared state; b, d represent annealed state).

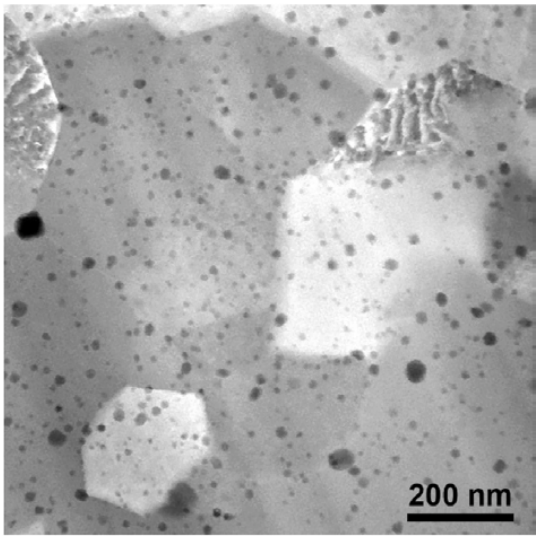

Fig. 13. STEM high-angle annular dark-field (HAADF) of the MA + SPS alloy after annealing at 800 °C for 100h. The dispersion of oxides remains high.

particles contrary to the FCC phase, which creates elongated particles, which, during prolonged annealing, underwent significant coarsening along with the former B2-BCC phase [54]. The precipitation of the σ-phase is related to a substantial increase in the hardness of the interdendritic region, also promoting its brittleness. In the end, it is the interdendritic region in which the crack propagates during the failure of the alloy [18]. To conclude, the precipitation of the σ-phase within the interdendritic region forming sort-of interconnected areas has a negative influence on the ductility, reducing the UCS. In addition, the formation of a higher volume fraction of the FCC phase and overall coarsening of the microstructure changes the course of the stress-strain curve around the CYS, making it less prominent.

The results of the compressive stress-strain testing at a high temperature of 800 °C are shown in Fig. 10c. It is evident that the temperature was extremely high for both samples and resulted in an enormous decrease in the CYS, especially for the MA + SPS sample. On the other hand, it allowed both samples to deform to higher strains due to continuous plastic deformation. The cast alloy achieved higher CYS however, after peaking out at 322 ± 30 MPa, the stress started to decrease gradually. On the other hand, the MA + SPS sample reached CYS of 147 ± 11 MPa and then gradually strengthened under plastic deformation. The alternative behaviour of the alloys signifies a different deformation mechanism. The activation of additional slip systems and deformation mechanisms at high temperatures caused the radical decrease in the CYS however, the sample still exhibited gradual work hardening during the plastic strain. The MA + SPS alloy has a very refined grain size, which contributes to the strengthening and more importantly, it is strengthened by carbides and nano oxides, which are stable at the temperatures of 800 °C and therefore contribute to the strengthening of the sample at high temperatures. On the contrary, the cast sample does not contain such structural constituents, thus after the yielding, the dislocations start moving through the sample without being hindered by a variety of particles found in MA + SPS alloy resulting in dynamic recovery, likewise, another B2-BCC structure alloy, as noted by Senkov et al. [42]. The total strain before the plastic deformation was nearly the same as in the case of the same alloy being

tested at RT, which signifies good chemical bonding among the structure of the sample compared to the MA + SPS alloy, where the plastic strain began at a lower stress. As Annasamy et al. [56] suggested for the $Al_{0.9}$CoCrFeNi alloy, the progressive stress reduction with increasing strain is caused by continuous dynamic recrystallization, resulting in continuous softening. This might be also a similar case for our alloy because of nearly identical chemical composition and phase composition, although the preparation techniques are different as Annasamy et al. [56] used arc melting and quenching. The softening may be also ascribed to modification of the interphase coherence, which might be distorted with the deformation [56].

4. Conclusion

In this study, an AlCoCrFeNi alloy was prepared by MA + SPS and by induction casting to compare the effect of the preparation method on the properties of the alloy. The results show that the AlCoCrFeNi alloy exhibits a combination of great mechanical properties with excellent oxidation resistance. Moreover, these attractive properties might be improved by the short-term MA + SPS, having a positive impact on the refinement of the microstructure and strength characteristics. The cast sample comprised a dendritic microstructure with the spinodal internal structure composed of 100 nm wide constituents of Al–Ni rich B2 ordered matrix and BCC Cr–Fe rich precipitates. On the contrary, the investigated MA + SPS alloy exhibited a three-phase composition detecting FCC in addition to the B2 and $Cr_{23}C_6$ phases. More importantly, the MA + SPS alloy exhibited ultrafine-grained microstructure of sub 500 nm grains, two orders of magnitude smaller than in the cast alloy. Substantial strengthening of the MA + SPS sample, supported by the presence of carbide particles, resulted in higher hardness by 130 HV and CYS by almost 700 MPa compared to the cast sample. However, the cast sample achieved a higher UCS of 3072 ± 122 MPa, accompanied by 29% plastic deformation. The MA + SPS sample showed excellent thermal stability when exposed to 800 °C, preserving its mechanical properties. The same cannot be said about the cast sample, as it underwent significant microstructure coarsening along with σ-phase precipitation, resulting in major ductility and UCS reduction.

Data availability

The data used in this article are available in the Zenodo repository: https://doi.org/10.5281/zenodo.10818463.

Declaration of competing interest

The authors declare that they have no known competing financial interests or personal relationships that could have appeared to influence the work reported in this paper.

Acknowledgement

This work was financially supported by the Czech Science Foundation (project No. 21-11313S). Additionally, the infrastructure used was made available through project No. CZ.02.01.01/00/22_008/0004631 - "Materials and Technologies for Sustainable Development," funded by the European Union and the state budget of the Czech Republic within the framework of the Jan Amos Komensky Operational Program.

Appendix A. Supplementary data

Supplementary data to this article can be found online at https://doi.org/10.1016/j.jmrt.2024.04.090.

References

[1] Yeh JW, et al. Nanostructured high-entropy alloys with Multiple principal elements: Novel alloy design concepts and Outcomes. Adv Eng Mater 2004;6(5):299–303.
[2] Hemphill MA, et al. Fatigue behavior of Al0.5CoCrCuFeNi high entropy alloys. Acta Mater 2012;60(16):5723–34.
[3] Senkov ON, Woodward CF. Microstructure and properties of a refractory NbCrMo0.5Ta0.5TiZr alloy. Mater Sci Eng 2011;529:311–20.
[4] Zhou YJ, et al. Solid solution alloys of AlCoCrFeNiTix with excellent room-temperature mechanical properties. Appl Phys Lett 2007;90(18):181904.
[5] Chen YY, et al. Microstructure and electrochemical properties of high entropy alloys—a comparison with type-304 stainless steel. Corrosion Sci 2005;47(9):2257–79.
[6] Lee C, et al. The effect of Boron on the corrosion resistance of the high entropy alloys Al[sub 0.5]CoCrCuFeNiB[sub x]. J Electrochem Soc 2007;154:C424–30.
[7] Wu P, et al. A non-equiatomic FeNiCoCr high-entropy alloy with excellent anti-corrosion performance and strength-ductility synergy. Corrosion Sci 2021;183:109341.
[8] Zhang Y, et al. High-entropy alloys with high Saturation Magnetization, Electrical Resistivity and Malleability. Sci Rep 2013;3(1):1455.
[9] Zuo TT, et al. Effects of Al and Si addition on the structure and properties of CoFeNi equal atomic ratio alloy. J Magn Magn Mater 2014;371:60–8.
[10] Chaudhary V, et al. Accelerated and conventional development of magnetic high entropy alloys. Mater Today 2021;49:231–52.
[11] Kao Y-F, et al. Microstructure and mechanical property of as-cast, -homogenized, and -deformed AlxCoCrFeNi (0≤x≤2) high-entropy alloys. J Alloys Compd 2009;488(1):57–64.
[12] Wang W-R, et al. Effects of Al addition on the microstructure and mechanical property of AlxCoCrFeNi high-entropy alloys. Intermetallics 2012;26:44–51.
[13] Yang T, et al. Effects of AL addition on microstructure and mechanical properties of AlxCoCrFeNi High-entropy alloy. Mater Sci Eng 2015;648:15–22.
[14] Li C, et al. Effect of aluminum contents on microstructure and properties of AlxCoCrFeNi alloys. J Alloys Compd 2010;504:S515–8.
[15] Ji W, et al. Mechanical alloying synthesis and spark plasma sintering consolidation of CoCrFeNiAl high-entropy alloy. J Alloys Compd 2014;589:61–6.
[16] Mohanty S, et al. Powder metallurgical processing of equiatomic AlCoCrFeNi high entropy alloy: microstructure and mechanical properties. Mater Sci Eng 2017;679:299–313.
[17] Rogal Ł, et al. Microstructure and mechanical properties of Al–Co–Cr–Fe–Ni base high entropy alloys obtained using powder metallurgy. Met Mater Int 2019;25(4):930–45.
[18] Munitz A, et al. Heat treatment impacts the micro-structure and mechanical properties of AlCoCrFeNi high entropy alloy. J Alloys Compd 2016;683:221–30.
[19] Chen Y-Y, et al. On the phase constituents of three CoCrFeNiX (X = B, Al, Ga) high-entropy alloys after prolonged annealing. J Alloys Compd 2022;900:163388.
[20] Qiao J, et al. Microstructural characteristics and mechanical Behaviors of AlCoCrFeNi high-entropy alloys at Ambient and cryogenic temperatures. Mater Sci Forum 2011;688:419–25.
[21] Wang YP, et al. Microstructure and compressive properties of AlCrFeCoNi high entropy alloy. Mater Sci Eng 2008;491(1):154–8.
[22] Otto F, et al. The influences of temperature and microstructure on the tensile properties of a CoCrFeMnNi high-entropy alloy. Acta Mater 2013;61(15):5743–55.
[23] Chae MJ, et al. Effect of light (X = Mg, Si) and heavy (X = Zn) metals on the microstructural evolution and densification of AlCuFeMnTi-X high-entropy alloy processed by advanced powder metallurgy. Powder Metall 2021;64(3):228–34.
[24] Sharma A, Lee H, Ahn B. Effect of additive elements (x = Cr, Mn, Zn, Sn) on the phase evolution and thermodynamic Complexity of AlCuSiFe-x high entropy alloys fabricated via powder metallurgy. Met Mater Int 2022;28(9):2216–24.
[25] Sharma A, Lee H, Ahn B. Tailoring compressive strength and absorption energy of lightweight multi-phase AlCuSiFeX (X = Cr, Mn, Zn, Sn) high-entropy alloys processed via powder metallurgy. Materials 2021;14. https://doi.org/10.3390/ma14174945.
[26] Linden Y, et al. Long-period antiphase domains and short-range order in a B2 matrix of the AlCoCrFeNi high-entropy alloy. Scripta Mater 2017;139:49–52.
[27] Tian Q, et al. The strengthening effects of relatively lightweight AlCoCrFeNi high entropy alloy. Mater Char 2019;151:302–9.
[28] Tokarewicz M, Grądzka-Dahlke M. Review of recent Research on AlCoCrFeNi high-entropy alloy. Metals 2021;11. https://doi.org/10.3390/met11081302.
[29] Hillel G, et al. Understanding the role of the constituting elements of the AlCoCrFeNi high entropy alloy through the investigation of quaternary alloys. Metals 2020;10. https://doi.org/10.3390/met10101275.
[30] Zhang Z, et al. Microstructure evolution and mechanical properties of CoCrFeNiAl0.3 high entropy alloy produced by ball milling in combination with thermomechanical consolidation. Mater Char 2022;187:111833.
[31] Cheng B, et al. Pressure-induced phase transition in the AlCoCrFeNi high-entropy alloy. Scripta Mater 2019;161:88–92.
[32] Geng Y, et al. Tribological performances of CoCrFeNiAl high entropy alloy matrix solid-lubricating composites over a wide temperature range. Tribol Int 2021;157:106912.
[33] Kleykamp H. Thermodynamic studies on chromium carbides by the electromotive force (emf) method. Journal of Alloys and Compounds - J ALLOYS COMPOUNDS 2001;321:138–45.
[34] Manzoni A, et al. Phase separation in equiatomic AlCoCrFeNi high-entropy alloy. Ultramicroscopy 2013;132:212–5.

[35] Tong C-J, et al. Microstructure characterization of AlxCoCrCuFeNi high-entropy alloy system with multiprincipal elements. Metall Mater Trans 2005;36(4):881–93.
[36] Munitz A, Meshi L, Kaufman MJ. Heat treatments' effects on the microstructure and mechanical properties of an equiatomic Al-Cr-Fe-Mn-Ni high entropy alloy. Mater Sci Eng 2017;689:384–94.
[37] Singh S, et al. Decomposition in multi-component AlCoCrCuFeNi high-entropy alloy. Acta Mater 2011;59(1):182–90.
[38] Rao Z, et al. Beyond solid solution high-entropy alloys: tailoring magnetic properties via spinodal decomposition. Adv Funct Mater 2021;31(7):2007668.
[39] Liu T-Y, et al. Spinodal decomposition and mechanical response of a TiZrNbTa high-entropy alloy. Materials 2019;12. https://doi.org/10.3390/ma12213508.
[40] Tang Y, et al. Effect of metastability on non-phase-transformation high-entropy alloys. Mater Des 2019;181:107928.
[41] Addepalli SN, et al. Effect of mechanical alloying on the microstructure of CoCrNiTiMox high entropy alloy. J Therm Spray Technol 2022;31(4):1045–55.
[42] Senkov ON, et al. Mechanical properties of an Al10Nb20Ta15Ti30V5Zr20 A2/B2 refractory superalloy and its constituent phases. Acta Mater 2023:119017.
[43] Shun T-T, Hung W-J. Effects of Cr content on microstructure and mechanical properties of $AlCoCr_xFeNi$ high-entropy alloy. Adv Mater Sci Eng 2018;2018:5826467.
[44] Baker I. A review of the mechanical properties of B2 compounds. Mater Sci Eng 1995;192–193:1–13.
[45] Jiao ZB, Luan JH, Liu CT. Strategies for improving ductility of ordered intermetallics. Prog Nat Sci: Mater Int 2016;26(1):1–12.
[46] Kainuma R, Ohtani H, Ishida K. Effect of alloying elements on martensitic transformation in the binary NiAl(β) phase alloys. Metall Mater Trans 1996;27(9):2445–53.
[47] Gale WF. Formation of twinned L12 type γ′ in alloys derived from the B2 β-NiAl structure. Intermetallics 1996;4(7):585–7.
[48] Xu Z, et al. Microstructure, mechanical properties, and wear behavior of AlCoCrFeNi high-entropy alloy and AlCrFeNi medium-entropy alloy with WC addition. Wear 2023;522:204701.
[49] Wei L, et al. Phase, microstructure and mechanical properties evaluation of AlCoCrFeNi high-entropy alloy during mechanical ball milling. Intermetallics 2021;138:107310.
[50] He JY, et al. A precipitation-hardened high-entropy alloy with outstanding tensile properties. Acta Mater 2016;102:187–96.
[51] Fu J, et al. Effect of mechanical alloying and spark plasma sintering on the microstructure and mechanical properties of ODS Eurofer. Mater Des 2019;177:107849.
[52] Průša F, et al. High-strength ultrafine-grained CoCrFeNiNb high-entropy alloy prepared by mechanical alloying: properties and strengthening mechanism. J Alloys Compd 2020;835:155308.
[53] Faraji A, et al. Microstructure, wear performance, and mechanical properties of spark plasma-sintered AlCoCrFeNi high-entropy alloy after heat treatment. Intermetallics 2022;149:107656.
[54] Strumza E, Hayun S. Comprehensive study of phase transitions in equiatomic AlCoCrFeNi high-entropy alloy. J Alloys Compd 2021;856:158220.
[55] Larsen SR, et al. Magnetic properties and thermal stability of B2 and bcc phases in AlCoCrFeMnxNi. J Alloys Compd 2021;861:158450.
[56] Annasamy M, et al. Dynamic recrystallization behaviour of AlxCoCrFeNi high entropy alloys during high-temperature plane strain compression. Mater Sci Eng 2019;745:90–106.